

# Topological confined massive surface states in strained bulk HgTe probed by RF compressibility

A. Inhofer,<sup>1</sup> S. Tchoumakov,<sup>2</sup> B.A. Assaf,<sup>3</sup> G. Fève,<sup>1</sup> J.M.  
Berroir,<sup>1</sup> V. Jouffrey,<sup>4</sup> D. Carpentier,<sup>4</sup> M. Goerbig,<sup>2</sup> B. Plaçais,<sup>1,\*</sup>

and

K. Bendias,<sup>5</sup> D.M. Mahler,<sup>5</sup> E. Bocquillon,<sup>5,1</sup> R. Schlereth,<sup>5</sup>  
C. Brüne,<sup>5</sup> H. Buhmann,<sup>5</sup> and L.W. Molenkamp<sup>5</sup>

<sup>1</sup>*Laboratoire Pierre Aigrain, Ecole Normale Supérieure,  
PSL Research University, CNRS, Université Pierre et Marie Curie,  
Sorbonne Universités, Université Paris Diderot, Sorbonne Paris-Cité,  
24 rue Lhomond, 75231 Paris Cedex 05, France*

<sup>2</sup>*Laboratoire de Physique des Solides,  
CNRS UMR 8502, Univ. Paris-Sud,  
Univ. Paris-Saclay F-91405 Orsay Cedex, France*

<sup>3</sup>*Département de Physique, Ecole Normale Supérieure-PSL Research University,  
CNRS, Université Pierre et Marie Curie-Sorbonne Universités,  
Université Paris Diderot-Sorbonne Paris Cité,  
24 rue Lhomond, 75231 Paris Cedex 05, France*

<sup>4</sup>*Univ. Lyon, ENS de Lyon, Univ. Claude Bernard,  
CNRS, Laboratoire de Physique, F-69342, France*

<sup>5</sup>*Faculty for Physics and Astronomy and Röntgen Center for Complex Material Systems,  
Universität Würzburg, Am Hubland, D-97074, Würzburg, Germany*

## Abstract

It is well established that topological insulators sustain Dirac fermion surface states as a consequence of band inversion in the bulk. These states have a helical spin polarization and a linear dispersion with large Fermi velocity. In this article we report on a set of experimental observations indicating the existence of massive surface states. These states are confined at the interface and dominate equilibrium and transport properties at high energy and/or high electric field. By monitoring the AC admittance of HgTe topological insulator field-effect capacitors, we access the compressibility and conductivity of surface states in a broad range of energy and electric fields. The Dirac surface states are characterized by a compressibility minimum, a linear energy dependence and a high mobility persisting up to energies much larger than the transport bandgap of the bulk. New features are revealed at high energies with signatures such as conductance peaks, compressibility bumps, a strong charge metastability and a Hall resistance anomaly. These features point to the existence of excited massive surface states, responsible for a strong intersubband scattering with the Dirac states and the nucleation of metastable bulk carriers. The spectrum of excited states agrees with predictions of a phenomenological model of the topological-trivial semiconductor interface. The model accounts for the finite interface depth and the effect of electric fields. The existence of excited topological states is essential for the understanding of topological phases and opens a route for engineering and exploiting topological resources in quantum technology.

## I. INTRODUCTION

Topological materials have emerged in the recent years [1] as a new class of matter with properties arising from peculiar crystal properties. These include topological insulators (TIs) with band inversion due to e.g. spin-orbit interaction [2,3], induced topological superconductors [1], and more recently topological semi-metals [4,5]. They have attracted strong attention as hosts of exotic excitations such as Majorana, Dirac or Weyl fermions, depending on symmetry and dimensionality. Topology also leaves macroscopic foot-prints like the Quantum Spin Hall Effect in 2D-TIs [6], the fractional Josephson effect in TI-SC junctions [7–9], and more recently the quantized Faraday rotation in 3D-TIs [10,11]. A thermodynamic approach to topological matter is needed if one wants to assess the robustness of topological protection for quantum manipulation purposes. Thermodynamics of topological matter has been considered so far essentially from the theoretical point of view [12,13]. Experimentally a first step consists in determining a phase diagram, based on susceptibility or transport coefficients measurements. Here we follow a standard approach already used to characterize the vortex state of superconductors [14–16]. We measure a broadband AC susceptibility, where the low and high frequency tails of the spectrum carry complementary information on the thermodynamic and transport coefficients. We focus here on the AC charge compressibility  $\chi(n, \mathcal{E}, \omega)$  to investigate the density - electric field ( $n$ - $\mathcal{E}$ ) diagram of topological surface states (TSSs) of 3D-TIs. Dealing with topological semiconductors, with a finite inversion bandgap  $\Delta$  ( $\Delta_{\Gamma_6-\Gamma_8} \simeq -0.3$  eV in HgTe), the topological character can be altered at high Fermi energy  $\mu \gg \Delta$ , and/or high electric field  $\mathcal{E} \sim \Delta/(e\xi)$ , where  $\xi \sim \hbar v_F/\Delta$  and  $v_F$  are TSS penetration depth and Fermi velocity. Using compressibility measurements we find evidence for a critical density  $n_T$  (or energy  $\mu_T$ ) for the nucleation of excited massive surface states (MSSs), and a critical field  $\mathcal{E}_T$  for the suppression of both TSSs and MSSs. Our results are supported by a theoretical model of the topological-trivial TI interface providing a comprehensive description of the combined effects of finite density and electric-fields.

To implement the experiment we rely on high quality strained bulk HgTe topological insulators, grown by molecular beam epitaxy (MBE), where TSS dominated quantum magnetotransport was previously reported [17–19]. It was found that TSSs screen an applied electric field over a broad range of doping energy exceeding the bulk band gap of HgTe [19]. This

phenomenon, called Dirac screening, addresses the question of the electronic compressibility of TSSs, where  $\chi(n, \mathcal{E}) = \partial n / \partial \mu$  is the charge susceptibility needed to close the electrostatic problem in the Poisson equation. Compressibility measurements have been considered so far mainly for the characterization of  $\text{Bi}_2\text{Se}_3$  thin crystals [20], and for the purpose of Landau-level spectroscopy in  $\text{HgTe}$  films [21]. Here we use metal-insulator-TI capacitors (MITI-Caps) and deduce the compressibility from the quantum capacitance correction,  $C_Q = e^2 \chi$ , to the insulator capacitance  $C_{ins}$  in the total capacitance  $C_{tot}$ .  $C_{tot}$  can be tuned by a DC gate voltage  $V_g$  controlling altogether the charge density  $n$  and the applied electric field  $\mathcal{E}$ . High frequency measurements ( $\lesssim 10$  GHz) give access to the dissipative regime, governed by the conductivity  $\sigma$ , and yield the diffusion constant  $\mathcal{D} = \sigma / C_Q$ . Thin insulators give access to high fields eventually exceeding the intrinsic field  $\Delta / e\xi \sim 10^8 \text{ Vm}^{-1}$  of  $\text{HgTe}$ .

We distinguish experimentally two field regimes exhibiting markedly different properties. At low field the quantum capacitance  $C_Q(\mu)$  and the diffusion constants  $\mathcal{D}(\mu)$  are reversible, exhibiting a minimum and a linear energy dependence which is reminiscent of Dirac states. The Dirac response extends in the electron regime over a broad range  $\Delta\mu \simeq 0.35 \text{ eV}$ , much larger than the transport bandgap ( $\sim 20 \text{ meV}$ ). In contrast, the situation is different at high fields where compressibility becomes strongly hysteretic, suggesting a metastable charge distribution with an admixture of bulk (BSs) and surface carriers (TSSs, MSSs). The transition is characterized by four observables: **i)** a bump in the compressibility, **ii)** a peak in conductivity (or  $\mathcal{D}$ ), **iii)** the onset of charge metastability and **iv)** a Hall resistance anomaly observed in complementary magneto-transport measurements. These signatures indicate the existence of a second type of carriers attributed to the massive surface state (MSSs) excited subbands acting as a new and efficient scattering channel for high mobility TSSs. MSSs have a different origin than electrostatically confined 2D electron states, in particular they persist at zero electric field.

To analyze the field-effect compressibility we rely on a heuristic theory of the topological - trivial insulator interface where the surface states are calculated by modeling the surface as a gradual interface between the inverted and direct semiconductors of bandgaps  $-2\Delta_1$  and  $2\Delta_2$  respectively. The model is similar to the one used for treating domain walls in 1D superconducting wires [22] and we include the effect of an applied electric field using Lorentz boosts as first discussed in Ref.[23]. This allows to obtain the spectrum of surface states at arbitrary electric field, which includes the helical massless Dirac fermion ground

state (TSSs) and a set of massive, spin degenerate, excited surface subbands (the above mentioned MSSs). In addition, the model predicts the existence of a critical electric field above which surface bound states disappear and the topological - trivial interface behaves as a normal semiconducting hetero-junction. It proves powerful in explaining the experimental phenomenology, in particular the observation of one or multiple scattering peaks whenever the Fermi energy crosses one or several MSS subband edges.

The paper is organized as follows. In section II we describe the MITI-Cap fabrication and the RF admittance measurement techniques. In section III we detail our experimental results. In section IV we detail the heuristic model of the field-effect compressibility of TIs. In section V we compare the model with experimental data. In section VI we conclude and discuss the implications of our findings for further understanding of TI thermodynamics.

## II. EXPERIMENTAL PRINCIPLES

The MITI-Caps are based on high mobility HgTe/CdHgTe hetero-structures (Figure1-a) grown by molecular beam epitaxy [17] where the HgTe layer, of thickness  $t_{HgTe} = 68$  nm, is strained by the CdTe insulating substrate so as to open a small bandgap  $\simeq 0.02$  eV in the topological HgTe layer between the light electron and heavy hole  $\Gamma_8$ -bands. The gap is smaller than the light electron- light hole ( $\Gamma_8$ - $\Gamma_6$ ) inverted bandgap,  $2\Delta_1 = \Delta_{\Gamma_6-\Gamma_8} \simeq -302$  meV [24]. We use a wet etching technique [25] to design a mesa and optical lithography to deposit contacts and define the gated area of the capacitor. A gold gate electrode is evaporated on top of a 10 nm-thin HfO<sub>2</sub> insulating layer, grown via low temperature atomic layer deposition (ALD) techniques. An ohmic contact, with a resistance  $R_c \simeq 50$  Ohms, is deposited by Ge/Au evaporation. A false color scanning electron microscopy (SEM) image of the gate-contact alignment is shown in Figure1-b. Two series of samples have been fabricated. Type A samples ( $S_A$ ) are covered by a 5 nm Cd<sub>0.7</sub>Hg<sub>0.3</sub>Te capping layer protecting the HgTe during the process and providing a well-defined trivial insulator boundary of band gap  $2\Delta_2^A \simeq 0.9$  eV [26,27] (Figure1-a). The total insulator thickness is  $t_{ins} = 15$  nm. Type B samples ( $S_B$ ) are devoid of capping layer and HfO<sub>2</sub> is directly deposited on HgTe (not shown in the figure). This entails an unintentional electron doping of the HgTe bulk (density  $n_0 \simeq 2.6 \cdot 10^{12}$  cm<sup>-2</sup> see below). The HgTe-HfO<sub>2</sub> interface involves an oxidized HgTe insulating layer of unknown and presumably small bandgap ( $\Delta_2^B < \Delta_2^A$ ). We have

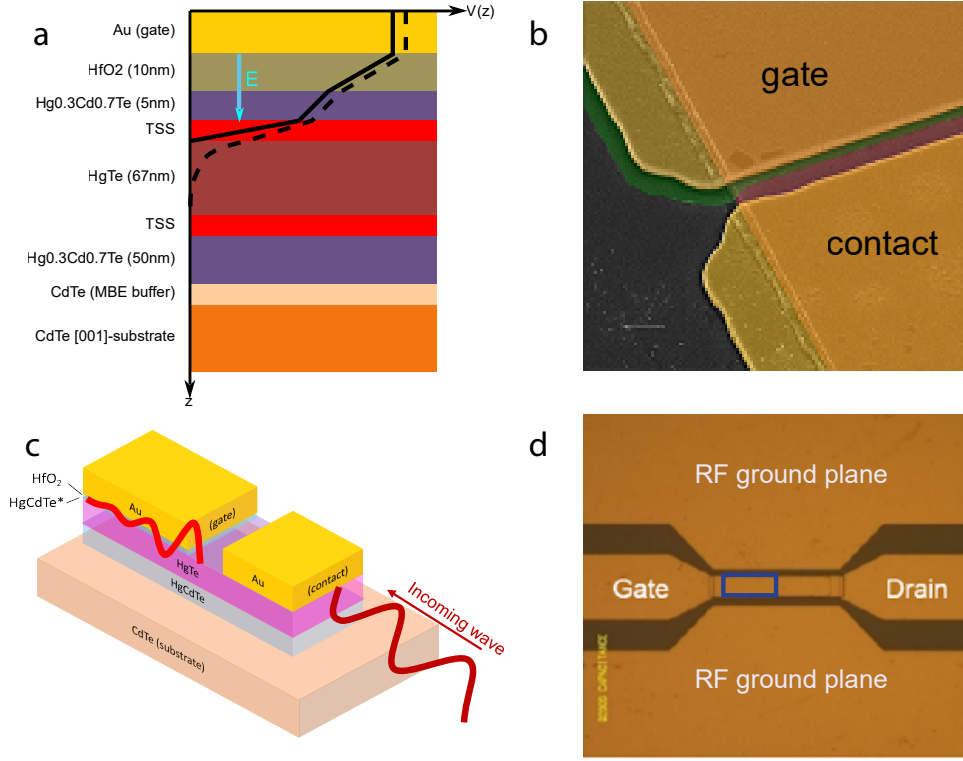


FIG. 1: Description of the MITI-Caps. a) sketch of a HgTe/Cd<sub>0.7</sub>Hg<sub>0.3</sub>Te capped heterostructure. Also shown in the figure are sketches of the electrostatic potential across the structure in the case of Dirac screening (solid line) and a mixed TSS and bulk state (BS) screening (dashed line). b) Colored SEM picture at a capacitor edge showing the gate and contact metallizations (gold), the HgTe mesa (purple) and the HfO<sub>2</sub> insulating layer (green). c) Sketch of the evanescent wave penetration of charge in the HgTe MITI-Cap when driven at RF frequency. d) optical image of the capacitor embedded in a coplanar wave guide. The  $44 \times 20 \mu\text{m}$  gated area is highlighted by a blue rectangle.

characterized in-situ the permittivity,  $\epsilon_{\text{HfO}_2} \simeq 3.6$ , of the thin oxide layer using a metal-oxide-metal (MOM) control capacitor. This value is process dependent and deviates here from to the accepted bulk value  $\epsilon_{\text{HfO}_2} \simeq 11.7$  [28]. Taking  $\epsilon_{\text{CdHgTe}} \simeq 8.5$  for the capping layer [26,27] we estimate the capacitance of our insulating stack  $C_{\text{ins}} = 2.65 \text{ mF/m}^2$  in agreement with our measurement below. The MITI-Caps are embedded in coplanar wave guides (Fig.1-d), designed for 0–40 GHz measurements. Five similar MITI-Caps of varied dimensions are fabricated per chip complemented by MOM, dummy and thru-line structures

used for calibration purpose (see below). For definiteness, experiments reported here refer to two capacitors of dimensions  $L \times W = 44 \times 20 \mu\text{m}$ , one of type  $A$  and one of type  $B$ .

Following earlier work on graphene [29] we primarily measure the electronic compressibility by vectorial network analyzer (VNA) techniques (frequency range  $\omega/2\pi = 50 \text{ kHz} - 8 \text{ GHz}$ ) in a cryogenic RF probe station at 10 K. Standard in-situ calibration techniques enable to de-embed the circuitry and the contact resistance contributions from the MITI-Cap admittance  $Y(\omega)$  of interest. The admittance spectrum  $Y(\omega)$  is accurately described by a distributed resistance-capacitance model [29],  $Y(\omega)/W = +jC_{tot}\omega L \times \tanh(\sqrt{j\sigma^{-1}C_{tot}\omega L^2})/\sqrt{j\sigma^{-1}C_{tot}\omega L^2}$ . With  $1/C_{tot} = 1/C_{ins} + 1/C_Q$  the measured quantum capacitance per unit area,  $C_Q = e^2\partial n/\partial\mu$  is a non-local compressibility where  $n$  stands for the total TI charge and  $\mu$  the value of the chemical potential at the TI surface. When two fluids are in mutual equilibrium, e.g. TSSs with BSs or TSSs with MSSs, they share the same surface chemical potential and their respective densities simply add in the total compressibility. The finite thickness of our HgTe-TI samples secures semi-infinite medium response, and the compressibility is the sum of the upper surface and semi-infinite bulk contributions. In the doped sample  $S_B$ , the sheet conductance includes a constant BS contribution which remains uniform over the bulk in the full frequency range.

Typical complex admittance spectra are shown in Figs.2-(a-c) for  $V_g = 0$  (Dirac point),  $V_g = 0.5, 3 \text{ V}$  (electron doped regime). We observe three regimes: quasi-stationary regime  $Y/W = jC_{tot}L\omega + (C_{tot}L\omega)^2\sigma^{-1}L/3$  (green shading), an intermediate regime (unshaded) and finally the evanescent wave regime (grey shading), where  $\Re(Y) \simeq \Im(Y) \simeq W\sqrt{C_{tot}\omega\sigma/2}$ . A remarkable frequency is the first  $[\Re(Y) = \Im(Y)]$  intercept at  $\omega_1 = \pi^2/(2C_{tot}\sigma^{-1}L^2) = 1 - 10 \text{ GHz}$  (lower limit of grey shading) corresponding to the commensurability of the evanescent wave with the sample length. The agreement between experimental spectra and the distributed RC line model (solid lines in Figs.2-(a-c)) is excellent and warrants the accuracy of the RF MITI-Cap approach to compressibility. The RC line model allows us to measure  $C_Q$  and  $\sigma$  (Fig.2-d), and thus extract  $\mathcal{D}$  via the Einstein relation (Fig.2-e). Accounting for the non-linear charge voltage characteristic we calculate the total electron density,  $n = \frac{1}{e} \int C_{tot}(V_g)dV_g$ . On subtracting the geometrical capacitance contribution ( $C_Q^{-1} = C_{tot}^{-1} - C_{ins}^{-1}$ ) we deduce the surface chemical potential,  $\mu = e \int C_{tot}/C_Q dV_g$ . Similarly we obtain the applied electric field  $\mathcal{E} = ne/(C_{inst}t_{ins})$ .

A similar chip using the same HgTe/CdHgTe hetero-structure is produced, hosting

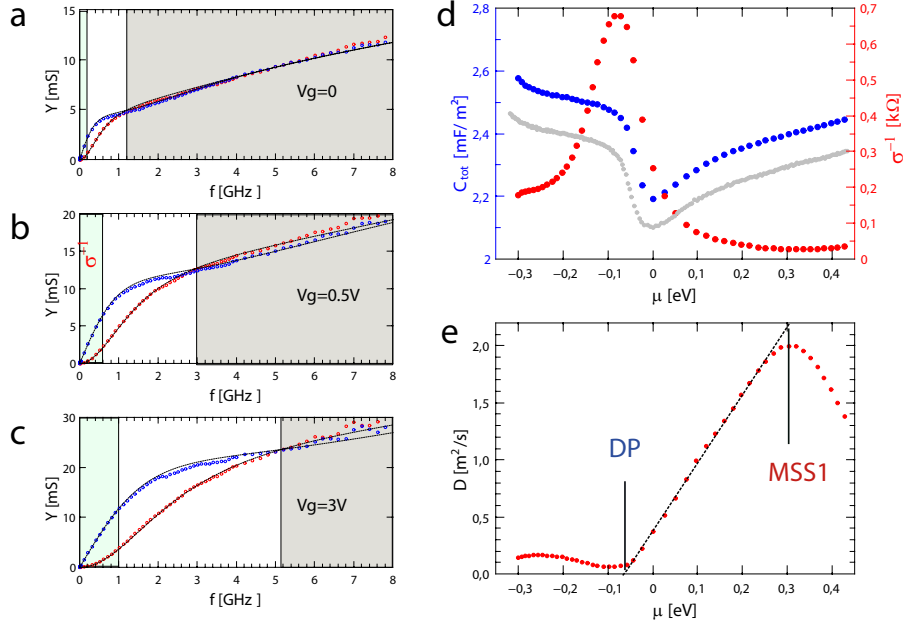


FIG. 2: RF measurement of the type-A MITI-Cap. Panel a-c) broadband spectrum of the MITI-Cap complex admittance  $Y(f)$  ( $\Re(Y)$  in red and  $\Im(Y)$  in blue) for three typical gate voltages. The quasi-stationary regime where  $Y/LW \simeq j\omega c - \sigma^{-1}(Lc\omega)^2/3$ , where  $c$  and  $\sigma^{-1}$  are the capacitance per unit area and the HgTe sheet resistivity, is shaded in green. The evanescent wave regime where  $Y/W \simeq (1+j)\sqrt{c\omega\sigma/2}$  is shaded in gray. d) the quantum capacitance  $C_Q$  and sheet resistance  $\sigma^{-1}$ , deduced from the fit of the AC-admittance spectra (solid lines in panel (a-c)), plotted as function of chemical potential in the reversible regime. The DC measurement from Fig.3-a (gray line) is added for comparison. The resistance shows an asymmetric peak close to neutrality. e) the diffusion constant  $\mathcal{D}(\mu)$  shows a dip at Dirac point (DP) and a linear increase in the electron regime corresponding to a TSS mobility  $\mu_e = 2e\mathcal{D}/\mu \simeq 12 \text{ m}^2\text{V}^{-1}\text{s}^{-1}$ . We observe a peak of  $\mathcal{D}(\mu)$  at  $\mu \approx 0.3 \text{ eV}$  signaling the onset of an additional and efficient scattering channel which we attribute below to the first excited surface subband (MSS1).

$600 \times 200 \text{ }\mu\text{m}$  Hall-bar structures, with the same optical lithography wet-etching technique equipped with a gold electrode as gate on top of 10 nm thick  $\text{HfO}_2$  insulator. Standard low frequency AC techniques in a four point measurement configuration are used at a temperature of 2 K in magnetic fields up to 2 T to measure the magnetic field and gate voltage  $V_g$  dependent longitudinal sheet resistance  $R_{xx}$  and Hall resistance  $R_{xy}$ . The carrier density  $n$



can be accessed in the classical Drude transport regime by the magnetic field dependence of the Hall resistance. Two samples of types *A* and *B* analog to the MITI-Cap samples with and without capping layer (not shown) were measured.

### III. EXPERIMENT

In this section we present a comprehensive set of field-effect AC charge compressibility measurements, complemented by DC hall bar measurements, that provide multiple evidence for the existence of excited topological surface states.

*Equilibrium compressibility.* Figures 3-a,b show the low-frequency capacitance, measured by the lock-in technique at 10 kHz, of  $S_A$  and  $S_B$  for two characteristic gate voltage cycling amplitudes:  $V_g^m = \pm 3$  V corresponding to the limits of the reversible charge response (dark blue and green lines for sample  $S_A$  and  $S_B$  respectively), and  $V_g^m = \pm 10$  V ( $V_g^m = \pm 7$  V) for the maximum amplitude sustainable by the insulating dielectric stack (light blue and green lines in Figs.3-a,b). For the large gate range sweeps we observe hysteresis loops with a butterfly shape and a trend toward capacitance saturation at large  $V_g$ . We use this asymptotic value (horizontal lines in Figs.3-a,b) as the experimental estimate of the insulator capacitance  $C_{ins}$ . Note that the reversible curves are themselves history dependent, the displayed ones corresponds to the first charging cycles after cool-down to  $T = 10$  K; reversible cycles subsequent to a high field charging are qualitatively similar but with a dip that is shifted in gate voltage and amplitude. We have checked that the MOM capacitance is linear and reversible in the same conditions suggesting that hysteresis essentially stems from the TI charging response. Issues concerning capacitance metastability are postponed for a discussion below and we first analyze the reversible charge response.

*Dirac fermion compressibility.* Reversible charging in both samples shows capacitance dips attributed to surface state neutrality. In sample  $S_A$  the dip is sharp and located at  $V_g = 0$ . In sample  $S_B$  it is smeared and shifted to  $V_g = -1.2$  V, corresponding to an n-type doping density  $n_0 = -2.6 \cdot 10^{12} \text{ cm}^{-2}$  (bulk donor density  $N_D = 4 \cdot 10^{17} \text{ cm}^{-3}$ ). On subtracting the insulator contribution  $1/C_{ins}$  and integrating the relevant quantities, we deduce the surface chemical potential  $\mu$  in the reversible state which is plotted in Figure 3-c (sample  $S_A$ ) as function of the applied electric field. The S-shape curve represents the charging path of the MITI-Cap in the  $\mu(\mathcal{E})$  representation. It is constrained by the Gauss relation and

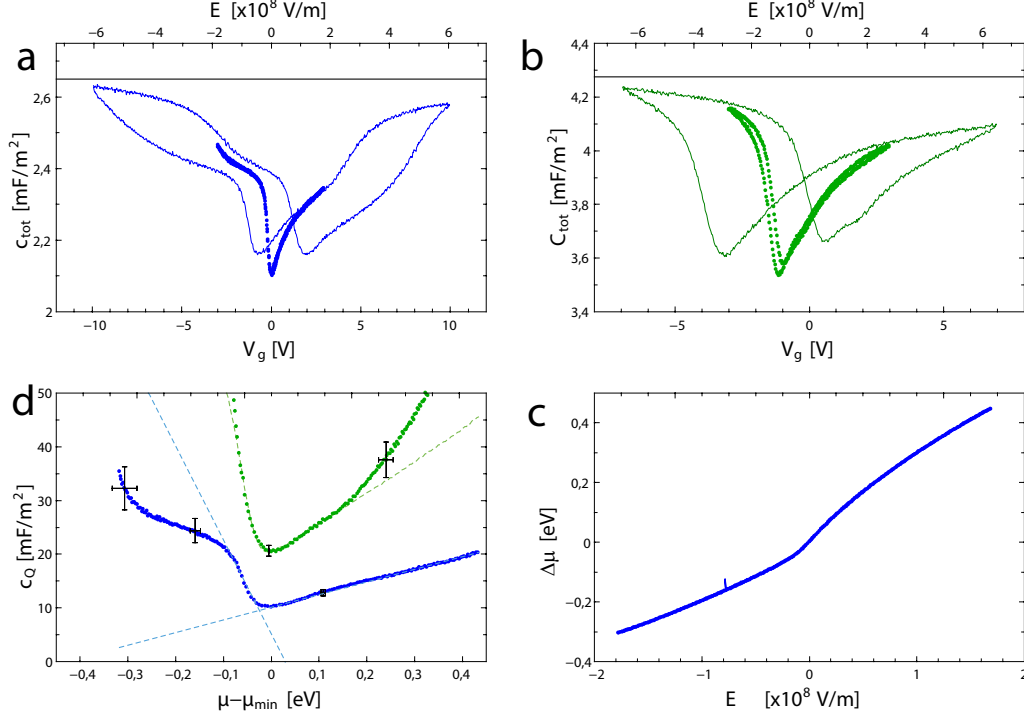


FIG. 3: DC measurement of the MITI-Caps. Gate voltage dependence of the capacitance in the undoped capped sample  $S_A$  (panel a) and the uncapped doped sample  $S_B$  (panel b). In both cases we distinguish a low electric field regime where  $C_{tot}(V_g)$  is reversible and a high field regime ( $V_g > 3V$ ) where MITI-Cap charging is hysteretic. Both sample show a capacitance dip in the reversible regime corresponding to the Dirac point of the upper surface state. It is shifted in sample  $S_B$ , indicating an electron-type chemical doping of density  $n \simeq 2.6 \cdot 10^{12} \text{ cm}^{-2}$ . From the capacitance saturation at large gate voltage we deduce the insulator capacitance  $C_{ins}^A \simeq 2.65 \text{ mF/m}^2$  and  $C_{ins}^B \simeq 4.27 \text{ mF/m}^2$ . Panel c) shows the surface chemical potential as function of the applied electric field. Panel d) shows the quantum capacitance for samples  $S_A$  and  $S_B$ . The error bars are calculated taking a 1% uncertainty in the determination of the insulator capacitance. The main feature is the linear  $C_Q(\mu)$  of sample  $S_A$  in the electron regime which is a direct signature of the intrinsic TI compressibility. It extends over a broad energy range  $\sim 0.3 \text{ eV}$ . Details of the analysis of  $C_Q(\mu)$  are given in the main text.

takes a simpler form,  $n(\mathcal{E}) = n_0 + t_{ins}C_{ins}\mathcal{E}/e$ , in the  $n(\mathcal{E})$  representation. Similar curves are obtained for sample  $S_B$  (not shown). Finally, Fig.3-d shows the reversible  $C_Q(\mu)$  plots of  $S_A$  (blue line) and  $S_B$  (green line). As expected from the additivity of compressibility in

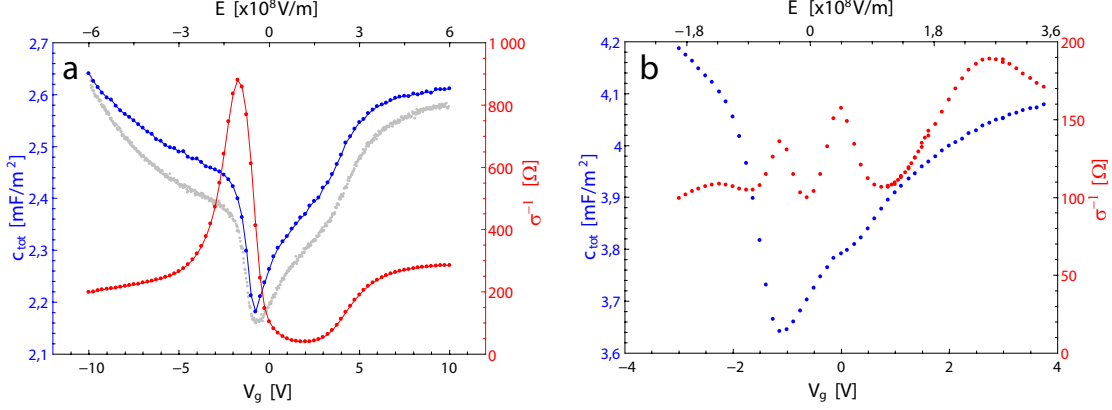


FIG. 4: High electric field capacitance and resistivity measurements in samples  $S_A$  (panel a) and  $S_B$  (panel b). The low-frequency data (gray dots in panel a) are added for comparison. To overcome hysteresis issues, the data correspond to the increasing gate voltage sweep. The most prominent features are the apparition of additional resistance peaks in the electron regime, the Dirac peak being signaled by the capacitance dip. In sample  $S_A$  the resistance peak is accompanied by a bump in the capacitance.

a two-fluid system, one has  $C_Q^B > C_Q^A$ . In order to quantify the effect of bulk carriers we have added in the figure the theoretical expectation (green dashed line) for the additional contribution of a trivial semiconductor with the above estimated dopant density  $N_D$ . From the good agreement with experiment we conclude that the  $C_Q(\mu)$  plot of sample  $S_A$  is a close estimate of the intrinsic TI response. The linear energy dependence precludes an interpretation of compressibility in terms of conventional massive surface states. In fact, its energy dependence can be mapped to a Dirac fermion density of state,  $C_Q = e^2\mu/(2\pi\hbar^2v_F^2)$ , taking  $v_F = 1.6 \cdot 10^6 \text{ ms}^{-1}$  in the electron regime and  $v_F = 0.5 \cdot 10^6 \text{ ms}^{-1}$  in the hole regime. These values are consistent with estimates deduced from ARPES experiments [30]. Remarkably, this Dirac-like response extends over a broad energy range ( $\mu = -0.05 \rightarrow +0.3 \text{ eV}$ ) widely exceeding the bulk transport bandgap. In the data reduction we have included a constant background  $\sim 10 \text{ mFm}^{-2}$  whose origin is not fully clarified. A possible explanation would be the nesting of the TSS Dirac point in the heavy-hole  $\Gamma_8$  branch, meaning that the observed compressibility minimum results from a superposition of electron TSS contribution with a heavy-hole  $\Gamma_8$  one.<sup>42</sup>

*Evidence of surface intersubband scattering.* We now turn to the RF susceptibility data.

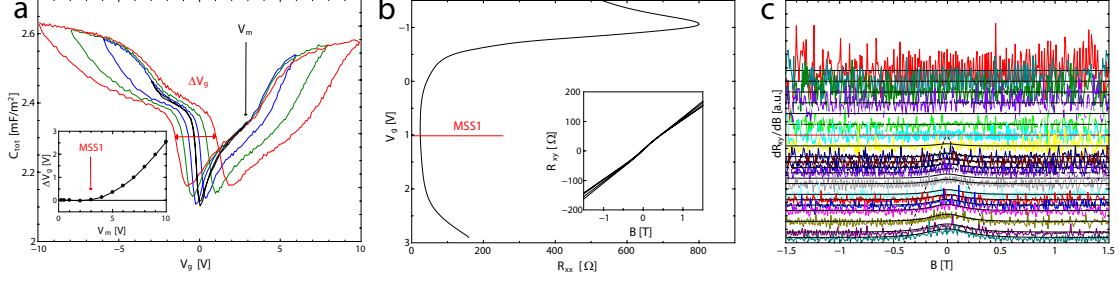


FIG. 5: Additional evidence of a transition at high electric field. Panel a) Hysteresis loops in sample  $S_A$  for increasing gate voltage sweep amplitudes  $V_m$  (rainbow colors). As seen in the inset, the width  $\Delta V$  of hysteresis loops sets in at  $V_g \geq 3$  V corresponding to the resistance minimum in Fig.4-a denoted as MSS1 and substantially increases above. Note also that the capacitance minima are shifted upward in the large  $V_g^m$  loops, indicating the presence of bulk carriers. Panel b) longitudinal resistance  $R_{xx}$  and Hall resistance  $R_{xy}$  (inset) measured in a type-A Hall bar. A secondary resistance peak is observed in  $R_{xx}$ , similar to that in Fig.4-a, which is accompanied by an S-shape anomaly in  $R_{xy}(B)$  (inset). The anomaly is highlighted in the  $dR_{xy}/dB(V_g)$  waterfall plot in panel c), where data are fitted by an empirical function  $\alpha/\cosh^2(B/B_0)$  (solid lines). As the anomaly onset coincides with the resistance minimum (red line), we conclude that a second type of carrier does nucleate at the conductivity maximum denoted as MSS1.

Fig.2-d shows  $C_{tot}(\mu)$  (blue dots) and  $\sigma^{-1}(\mu)$  (red dots) deduced from admittance spectra in sample  $S_A$  in the reversible regime. The DC capacitance (grey dots) has been reproduced for comparison of the two techniques. The good agreement, beside a small amplitude shift due to calibration issues, shows that compressibility is frequency independent, confirming our analysis of admittance spectra that dissipative effects mainly stem from finite conductivity and not from an intrinsic  $\chi(f)$  dependence. The resistivity exhibits a Dirac-like peak (DP) which is slightly shifted with respect to the capacitance dip, supporting our conjecture that the DP is nested in the  $\Gamma_8$  band. The shape of the resistance reflects the electron-hole asymmetry of HgTe. We have plotted in Fig.2-e the diffusion constant  $\mathcal{D}(\mu) = \sigma/C_Q$  in sample  $S_A$ . We observe a minimum at  $\mu \simeq -0.05$  eV and a linear increase in the electron regime up to  $\mu \simeq 0.3$  eV, corresponding to a constant mobility  $\mu_{TSS} = 2e\mathcal{D}/\mu \simeq 12 \text{ m}^2\text{V}^{-1}\text{s}^{-1}$ . This large value is characteristic of massless Dirac fermions and comparable with values deduced from magneto-transport experiments [19]. The function  $\mathcal{D}(\mu)$  being a

marker of the scattering mechanism, the linear dependence is indicative of a screened charge disorder [41]. Remarkably we see a drop of  $\mathcal{D}(\mu)$  at  $\mu \simeq 0.3$  eV giving rise to a well defined *diffusion-constant peak*. This peak will be used below to define a boundary of the topological phase (MSS1 subband edge).  $C_Q$  being monotonic in the same energy range, the peak in  $\mathcal{D}(\mu)$  reflects the peak in  $\sigma(\mu)$ . Fig.4-a is an extension of Fig.2-d at the maximum gate voltage span, taking the upward voltage sweep of the hysteresis loops. It shows that the conductance peak evolves into a resistance plateau at large electric field.

The phenomenology is even richer in  $S_B$  (Fig.4-b) where we observe, besides the Dirac peak, *two resistance peaks* in the electron regime (also seen in type-B Hall bars) and a faint one in the hole regime. In sample  $S_A$  (Fig.4-a) the resistance peak is accompanied by a bump in the capacitance, seen both in the RF (red dots) and DC (grey dots) data, reflecting the onset of a secondary carrier contribution. As mentioned above, compressibility features in sample  $S_B$  are blurred by bulk carrier contributions and bumps are hardly visible.

*Excited subbands and charge metastability.* In Fig.5 we analyze two complementary aspects of the TI charging phenomenology. Fig.5-a shows a set of hysteretic charging characteristics  $C_{tot}(V_g)$  for increasing gate voltage amplitudes  $V_g^m$  in sample  $S_A$ . They have a butterfly shape with two capacitance minima that are shifted upward or backward depending on the direction of the voltage sweep. We attribute this metastability to the nucleation of bulk carriers at high electric field, either electrons or holes depending on the field history. The loop width,  $\Delta V_g(V_g^m)$  (inset) sets-in at  $V_g^m \simeq 3$  V and gradually increases up to  $\Delta V_g \simeq 3$  V at  $V_g^m \simeq 10$  V, corresponding to a bulk charge variation  $\Delta n_B = \pm 2 \cdot 10^{12} \text{ cm}^{-2}$ . Note that the capacitance minima are shifted upward at large  $V_g^m$  supporting the contribution of additional bulk carriers in the compressibility.

*Excited subbands and secondary charge carriers.* Figs.5-b,c show the  $R_{xy}$ ,  $R_{xx}$  magnetotransport measurements performed in a type-A Hall bar. The capped sample shows a clear maximum of the sheet resistance in dependence of the applied gate voltage  $V_g$ , accompanied by a change in the sign of the Hall resistance (not shown) indicating the state with lowest carrier density at  $V_g \approx -1.0$  V. Increasing the gate voltage (electron density) decreases the sheet resistance  $\sigma^{-1}$  up to  $V_g \approx 1.0$  V. For higher gate voltages  $\sigma^{-1}$  increases monotonically with  $V_g$  (Fig.5-c) and a non-linearity in the Hall resistance develops for low magnetic fields (inset of Fig.5-b). The uncapped sample consistently shows additional peaks in the longitudinal resistance (not shown), with the only difference, that the p-conducting regime could

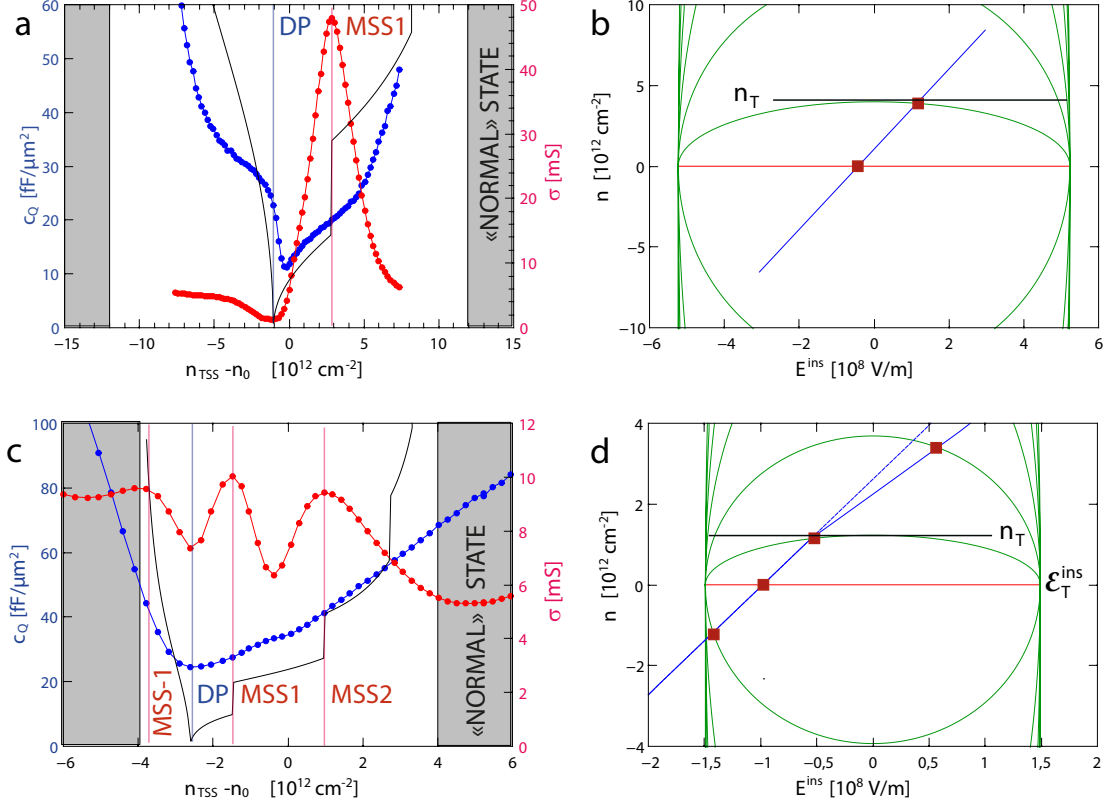


FIG. 6: Density - electric field phase diagram of strained bulk HgTe. The compressibility-conductance data (blue-red data points) from samples  $S_A$  (panel a) and  $S_B$  (panel c), are compared with prediction of the model in Section IV. By adjusting the resistance peak positions with respect to Dirac point we deduced the model parameters (see the text). The MITI-Cap charging paths are included in the  $n$ - $\mathcal{E}$  phase diagram as depicted in panels b) and d). From this analysis we deduce the critical electric field of the TI :  $\mathcal{E}_T^A = 2.64 \cdot 10^8 \text{ Vm}^{-1}$  and  $\mathcal{E}_T^B = 0.81 \cdot 10^8 \text{ Vm}^{-1}$ . The strong reduction of  $\mathcal{E}_T$  in  $S_B$  is due to the absence of a capping layer. Above  $\mathcal{E}_T$ , the topological-trivial insulator interface behaves as a normal, non-topological, interface. Below  $\mathcal{E}_T$ , the transition to a normal-like behavior is gradual and involves the population of excited massive surface states. Two such subbands can be seen in  $S_B$  due to chemical doping and a lower excitation gap.

not be reached in the available gate voltage range due to the high (unintentional) n-doping. Beside the Dirac peak (at  $V_g = -1.1 \text{ V}$ ),  $R_{xx}(V_g)$  exhibits a secondary peak (at  $V_g \simeq 3 \text{ V}$ ) reminiscent of the one observed in the capacitor measurement of Fig4-a. The Hall resistance  $R_{xy} \propto B$  develops an anomaly for  $V_g \gtrsim 1 \text{ V}$  (inset of Fig.5-b) signaling the advent of a secondary carrier type. The anomaly is best depicted by plotting the derivative  $\partial R_{xy}/\partial B$

in Fig.5-c, where the base line is shifted according to the applied gate voltage. Data are fitted using an empirical function  $\alpha/\cosh^2(B/B_0)$  (solid lines) used to extract the magnetic field range  $B_0$  of the anomaly. We find  $B_0 \propto (V_g - V_{g1})$  with  $V_{g1} = 1.0$  V corresponding to the resistance minimum in that sample. Similar analysis has been carried out in type-B samples where we observe multiple  $R_{xx}$  peaks (not shown), also reminiscent of the capacitor measurement in Fig.4-b.

*Density-electric field phase diagram.* In conclusion of the experimental part of the paper we have observed in undoped HgTe TI capacitors ( $S_A$ ) the existence of a characteristic field signaled by a conductivity peak (Fig.2-d), or a resistance minimum (Fig.4-a, Fig.5-c), a bump of compressibility (Fig.4-a), the onset of metastability (Fig.5-a), and a Hall resistance anomaly (Fig.5-b) typical of a secondary carrier contribution. Similar behavior is observed in the doped sample  $S_B$  with an even richer phenomenology. The main results of the paper are summarized in Fig.6 which includes the  $C_Q(n), \sigma(n)$  plots in Fig.6-a (sample  $S_A$ ) and Fig.6-c (sample  $S_B$ ), and a density-electric field phase diagram in Figs.5-(b,d) where the positions of the Dirac and scattering peaks are reported, together with the charging lines of the MITI-Caps. These diagrams will be used for a direct comparison with the theory below (green-lines). Our results suggest that the onset of metastability in the charge-electric field phase diagram is linked to the possible nucleation of additional surface subbands. The origin of these subbands will be theoretically investigated in the next section.

#### IV. THEORY

In this section, we describe the topological-normal junction giving rise to surface states over a penetration depth  $\xi$  within a simplified effective four-band model and a gradual interface of length  $\xi$  between the topological (inverted-gap) and the trivial (normal-gap) insulator. We obtain the Dirac fermion TSS ground state, a set of excited surface states (MSSs) and consider the effect of an applied electric field on the surface-states spectra. Our theoretical findings are then corroborated with numerical  $k \cdot p$  calculations of a gradual junction using six-band models particularly designed for HgTe.

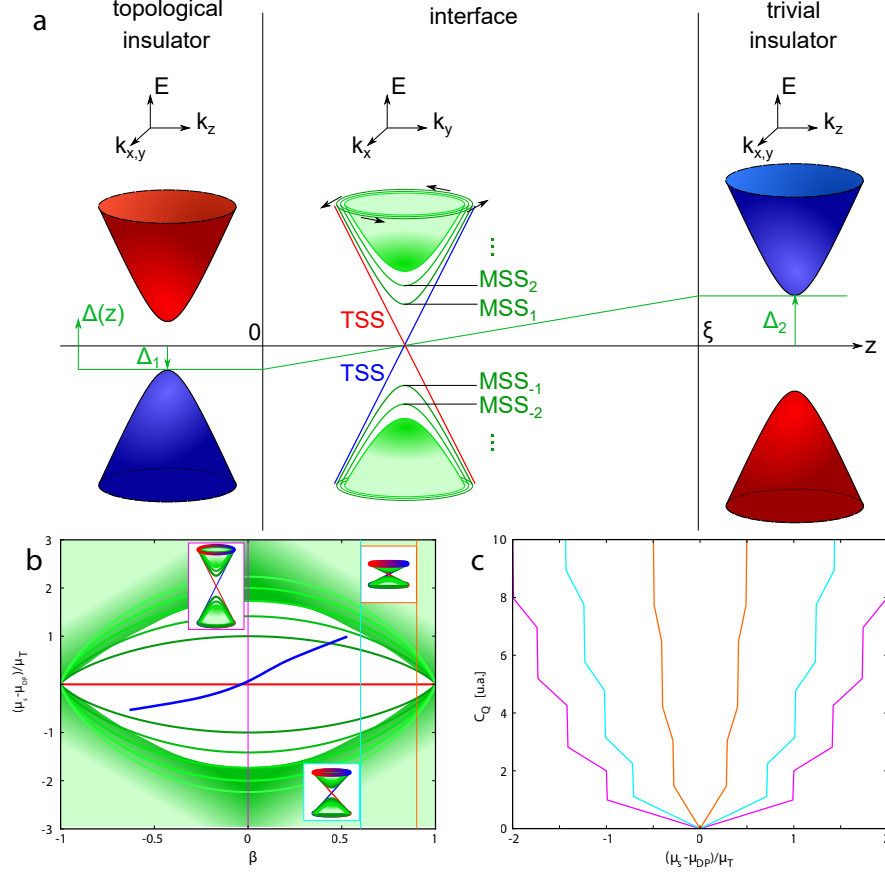


FIG. 7: Model of massive surface states (MSSs) in topological insulators. Panel a) Simplified model for the interface of a topological insulator (on the left) and a normal insulator (on the right). In the interface one observes multiple surface states. Panel b) Band gaps of the TSS and MSS as a function of the reduced electric field  $\beta = \mathcal{E}/\mathcal{E}_T$ . The blue solid line is a sketch of a capacitor charging line measured in Fig.3-c. Panel c) Illustration of the double effect of electric field in the quantum capacitance  $C_Q(\mu, \mathcal{E})$  for selected values of the parameters represented by colored lines in panel b). The group velocity of the Dirac fermion decreases with increasing electric field and its density of states rises up to the critical field with a vanishing of the Fermi velocity  $C_Q(\mu)\mathcal{E} \rightarrow \infty$  at the critical field  $\mathcal{E}_T$ . At finite doping the subbands cross the Fermi energy at  $\mathcal{E} < \mathcal{E}_T$  giving rise to a stepwise increase of  $C_Q(\mathcal{E})_{\mu=Cte}$ .



### A. Effective model of surface states

In order to model the insulating phases, we use the simplified linear four-band  $k \cdot P$ -Hamiltonian describing the bands around the  $\Gamma$ -point of an inverted band structure [1]

$$\hat{H}_0(\mathbf{k}, \Delta) = \begin{bmatrix} \Delta & \hbar v_F k_y & 0 & \hbar v_F(k_z - ik_x) \\ \hbar v_F k_y & -\Delta & \hbar v_F(k_z - ik_x) & 0 \\ 0 & \hbar v_F(k_z + ik_x) & \Delta & -\hbar v_F k_y \\ \hbar v_F(k_z + ik_x) & 0 & -\hbar v_F k_y & -\Delta \end{bmatrix}, \quad (1)$$

for which the spectrum consists of two doubly degenerate bands  $\varepsilon_k^{(\pm)} = \pm \sqrt{\Delta^2 + \hbar^2 v_F^2 k^2}$ . This spectrum is independent of the sign of the gap parameter  $\Delta$ . In the following we model HgTe as an inverted insulator of gap  $-\Delta_1 < 0$  that is in contact with a normal insulator of gap  $\Delta_2 > 0$ . The corresponding bulk Hamiltonians are  $\hat{H}_0(\mathbf{k}, -\Delta_1)$  and  $\hat{H}_0(\mathbf{k}, \Delta_2)$  as represented on the left- and right-hand sides of panel (a) of Fig. (6).

We consider that HgTe is located in a region  $z < 0$  and that the normal insulator (CdHgTe or HfO<sub>2</sub>) is located at  $z > \xi$ . We model the interface  $0 < z < \xi$  between the two semi-conductors using an interpolating Hamiltonian  $\hat{H}_{s0} = \hat{H}_0[\mathbf{k}, -\Delta_1 + e\mathcal{E}_T z]$  with the characteristic field

$$\mathcal{E}_T = \frac{\Delta_1 + \Delta_2}{e\xi}. \quad (2)$$

This field plays the role of a confinement or gap field that we have chosen to have the same physical dimension as an electric field. The evolution of the gap is sketched as a green line in panel (a) of Fig. 6 and can be viewed as a three-dimensional generalization of the procedure described in Ref. [22] for a one-dimensional system and in Ref. [32] for Weyl semimetals. This Hamiltonian contains a pair of non-commuting variables  $[z, k_z] \neq 0$  that can be merged into the same matrix elements with the help of a  $k$ -independent unitary transformation  $|\Psi\rangle = \hat{U}|\Psi'\rangle$ . One finds in this new basis

$$\hat{H}'_{s0} = \hat{U}^\dagger \hat{H}_{s0} \hat{U} = \begin{bmatrix} \hbar v_F k_x & \hbar v_F k_y & 0 & \sqrt{2\hbar v_F e \mathcal{E}_T} \hat{a}^\dagger \\ \hbar v_F k_y & -\hbar v_F k_x & \sqrt{2\hbar v_F e \mathcal{E}_T} \hat{a}^\dagger & 0 \\ 0 & \sqrt{2\hbar v_F e \mathcal{E}_T} \hat{a} & \hbar v_F k_x & -\hbar v_F k_y \\ \sqrt{2\hbar v_F e \mathcal{E}_T} \hat{a} & 0 & -\hbar v_F k_y & -\hbar v_F k_x \end{bmatrix}, \quad (3)$$

where we have introduced the ladder operators  $\hat{a} = [\hbar v_F k_z - i(e\mathcal{E}_T z - \Delta_1)] / \sqrt{2\hbar v_F e \mathcal{E}_T}$  and  $\hat{a}^\dagger = [\hbar v_F k_z + i(e\mathcal{E}_T z - \Delta_1)] / \sqrt{2\hbar v_F e \mathcal{E}_T}$  such that  $[\hat{a}, \hat{a}^\dagger] = 1$ . This Hamiltonian is similar

to that in a magnetic field [33] and we introduce the number states  $|m\rangle$  associated to the number operator  $\hat{m} = \hat{a}^\dagger \hat{a}$ , with  $\hat{m}|m\rangle = m|m\rangle$ . These states are localized around the mean position  $\langle z \rangle = \Delta_1/e\mathcal{E}_T = \Delta_1\xi/(\Delta_1 + \Delta_2) \in [0, \xi]$  since by definition  $\Delta_1, \Delta_2 > 0$ . Notice that these states are located outside the interval  $[0, \xi]$  if there is no gap inversion, *i.e.* if  $\Delta_1/\Delta_2 < 0$ .

For  $m \geq 1$  one finds an infinite number of states of the form  $|\Psi_{m,\mathbf{k}}\rangle = (\alpha_1|m\rangle, \alpha_2|m\rangle, \alpha_3|m-1\rangle, \alpha_4|m-1\rangle)$ . Their band dispersion is doubled in that one finds, for each value of  $m$ , a band at positive and negative energy,  $\varepsilon_{m,k_x,k_y}^{(\pm)} = \pm\sqrt{\hbar^2 v_F^2(k_x^2 + k_y^2) + 2\hbar v_F e \mathcal{E}_T m}$ , with a gap similar to that in a magnetic field  $\Delta E \sim \sqrt{2\hbar v_F e \mathcal{E}_T m}$ . In addition, these bands are doubly degenerate. These massive surface states (MSS) depend explicitly on the characteristic field  $\mathcal{E}_T$  and thus on the parameters characterizing the interface. In the limit of a sharp surface, *i.e.*  $\xi \rightarrow 0$  so that  $\mathcal{E}_T \rightarrow \infty$ , these bands are shifted to high energies and do not play any physical role.

In contrast to these bands, the  $m = 0$  surface states are not twofold degenerate. It is of the form  $|\Psi_{0,\mathbf{k}}\rangle = (\alpha_1|0\rangle, \alpha_2|0\rangle, 0, 0)$  and its energy dispersion is that of a two-dimensional Dirac cone  $\varepsilon_{0,k_x,k_y}^{(\pm)} = \pm\hbar v_F \sqrt{k_x^2 + k_y^2}$ . It is independent of  $\mathcal{E}_T$  and one can show [32] that this state is of topological nature. This topological surface state (TSS) survives in the limit of an infinitely sharp interface, as expected, and shows a dispersion that only depends on the bulk parameter  $v_F$ , in agreement with previous studies [1]. We represent the spectra of the  $\text{MSS}_{\pm m}$  states and the TSS state in panel (a) of Fig. 7.

Most saliently, the MSS can be modified to great extent by an electric field applied perpendicular to the surface. As an effect of charge screening, the associated electrostatic potential drops in the interface and generates an electric field  $\boldsymbol{\mathcal{E}} \equiv -\mathcal{E}\mathbf{e}_z \approx -V_g/\xi\mathbf{e}_z$ . The interface Hamiltonian, for  $0 < z < \xi$ , is now  $\hat{H}_s = \hat{H}'_{s0} + (V_0 - e\mathcal{E}z)\mathbb{1}$ . Notice that the added term remains invariant under the above-mentioned rotation that leads to the form of the Hamiltonian given by Eq. (3). As detailed in App. VII, the spectrum now depends on the ratio  $\beta = \mathcal{E}/\mathcal{E}_T$  between the applied and the characteristic electric fields. The spectrum for the  $m \geq 1$  states is still doubly degenerate with the dispersion relations  $\varepsilon_{m,k_x,k_y}(\beta) = \sqrt{(1 - \beta^2)\hbar^2 v_F^2(k_x^2 + k_y^2) + 2(1 - \beta^2)^{3/2}\hbar v_F e \mathcal{E}_T m}$ . One observes that the gap is reduced by the applied electric field  $\Delta E(\beta) \sim (1 - \beta^2)^{3/4}\sqrt{2\hbar v_F e \mathcal{E}_T m}$  and that the dispersion relation flattens out because of the reduced Fermi velocity that vanishes at  $\mathcal{E}_T$ . The special  $m = 0$  surface state is also flattened and one finds  $\varepsilon_{0,k_x,k_y}^{(\pm)} = \pm(1 - \beta^2)^{1/2}\hbar v_F \sqrt{k_x^2 + k_y^2}$ . In

panel (b) of Fig. 7 we represent the extrema of the  $\text{MSS}_{\pm m}$  (in green) and of the TSS at  $k_x = k_y = 0$  (in red) as a function of  $\beta = \mathcal{E}/\mathcal{E}_T$ . We observe that the MSS merge for an electric field close to the critical field  $\mathcal{E}_T$ . Beyond this limit our model (5) has no bound state so that the interface behaves as a conventional semiconducting heterojunction. This shows that  $\mathcal{E}_T$  is not only a characteristic field governing the excited state spectrum but actually a genuine critical field for the topological nature of the interface. The applied electric potential also influences the chemical potential [blue line in Fig. (7)] that will eventually cross the MSS. This leads to the experimentally observed kinks in the compressibility and features in the conductivity that we discuss in detail in the following section.

We finish this theoretical section with a discussion of the density of states  $\rho(\epsilon)$ , which is directly proportional to the quantum capacitance (at  $T = 0$ ). The density of states associated with the surface states per unit area reads

$$\rho(\epsilon) = \frac{|\epsilon|}{2\pi\hbar^2 v_F^2 (1 - \beta^2)} \sum_l \Theta \left[ |\epsilon| - (1 - \beta^2)^{3/4} \sqrt{2\hbar v_F e \mathcal{E}_T m} \right], \quad (4)$$

where  $\Theta(x)$  is the Heaviside function. The corresponding behavior of the quantum capacitance is represented in panel (c) of Fig. 7 for typical values of  $\beta = \mathcal{E}/\mathcal{E}_T$ . One observes that the gaps are smaller and that the density of states becomes enhanced for larger electric fields (in red). This is a direct consequence of the reduced Fermi velocity in the presence of an electric field, as pointed out above. Notice, however, that in the experimental setup the chemical potential depends itself on the applied electric potential and therefore jumps from one curve to the other.

## B. Numerical $k \cdot P$ treatment of surface states

To complement the previous analytical study, we have performed a numerical study of the band structure of an HgTe/CdTe interface, based on a  $k \cdot P$  model. Our numerical approach amounts discretizing a standard Kane model for the 6 bands  $\Gamma_{6,\pm 1/2}, \Gamma_{8,\pm 1/2}, \Gamma_{8,\pm 3/2}$  hamiltonian with known parameters for HgTe and CdTe from the literature<sup>37</sup>. This Kane model is then discretized, with parameters interpolating between their values in both materials over a distance  $\xi$ , corresponding to the size of the interface. This description incorporates the stress induced by the lattice mismatch through a Bir-Pikus term. The resulting band structure is shown in Fig.8, where the color encodes the eigenstate's density around the

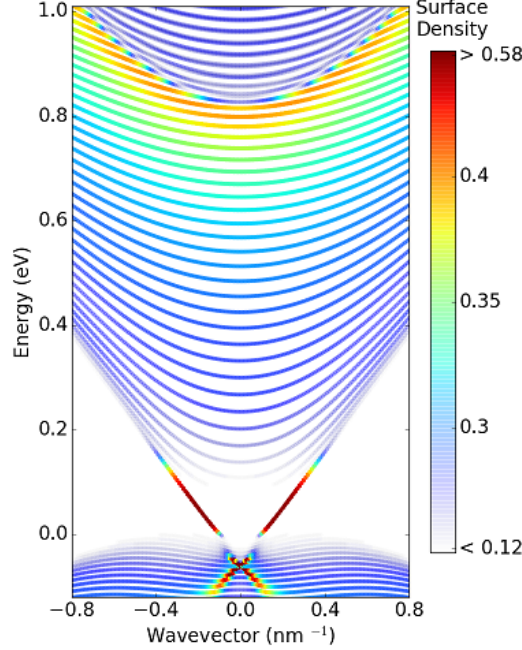


FIG. 8: Numerical dispersion relation  $E(k_{\parallel})$  for an HgTe/CdTe interface obtained within a 6-band Kane model.  $k_{\parallel}$  corresponds to the momentum along the interface. The color encodes the density of eigenstates in a region of  $\sim 6$  nm around the interface. The existence of localized states around the interface is shown within the gap but also at high energy around 1 eV.

HgTe/CdTe interface. The band structure is calculated for an HgTe thickness of 70 nm and  $\xi = 5$  nm. Note that this band structure is obtained at zero electric field and using CdTe ( $2\Delta_2 \simeq 1.5$  eV) as a capping layer boundary. We find a massive surface subband at 1 eV which is accompanied by a strong depletion of the bulk state amplitude in the surface layer that confirms the above picture of high energy surface states (MSSs). The excitation energy is quite large (still smaller than  $2\Delta_2$ ) and found to be sensitive to the detail of the shape of the smooth interface. This is consistent with the analytical approach of section IV A which focussed on a linear interpolation between the two materials and neglects asymmetry between the two materials beyond the gap inversion. We stress that these MSSs are predicted at zero electric field, and assume that they follow the electric field dependence predicted by the approach of section IV A.

## V. COMPARISON WITH EXPERIMENT

We turn back to Fig.6 where experimental data are summarized and the conductance peak positions (red squares) compared with the theoretical model of the massive surface subbands (green lines) in a density - electric field  $n$ - $\mathcal{E}$  phase diagram. In the model there is no bulk charge involved and  $n$  refers to the surface state density only. The sub-band minima obey  $n_m = n_T \times \frac{m(m+1)}{2} \sqrt{1 - \beta^2}$  where  $n_T = e\mathcal{E}_T/2\pi\hbar v_F$  and  $\beta = \mathcal{E}_{\text{HgTe}}/\mathcal{E}_T$ ;  $\mathcal{E}_{\text{HgTe}}$  is the local field in the HgTe surface layer which differs from the applied field  $\mathcal{E}$  by a factor  $\varepsilon_{\text{ins}}/\varepsilon_{\text{HgTe}}$ . Accounting for the capacitor charging line  $n = n_0 + t_{\text{ins}}C_{\text{ins}}\mathcal{E}/e$  where  $n$  is the total TI charge and  $n_0$  the chemical doping, one has only access to a line cut of the  $n$ - $\mathcal{E}$  diagram in a given device. Having two samples with different doping one could think of mapping further the  $n$ - $\mathcal{E}$  diagram. However  $S_A$  and  $S_B$  also have different capping so that they cannot be compared directly and we analyze their diagrams separately in Fig.6-b and Fig.6-d.

As seen in the figures, the model explains qualitatively the observed conductance peaks and their position relative to the Dirac point. In sample  $S_A$ , the density at the first subband intercept,  $n_1 - n_{DP} \simeq 4 \cdot 10^{12} \text{ cm}^{-2}$  ( $\mathcal{E}_1 = 1.15 \cdot 10^8 \text{ Vm}^{-1}$ ), is large so that the predicted second subband, at  $n_2 \simeq 3n_1 \simeq 12 \cdot 10^{12} \text{ cm}^{-2}$ , remains at the border of our experimental window. In the doped sample  $S_B$ , we observe two conductance peaks, at negative ( $\mathcal{E}_1 = -0.55 \cdot 10^8 \text{ Vm}^{-1}$ ) and positive ( $\mathcal{E}_2 = +0.6 \cdot 10^8 \text{ Vm}^{-1}$ ) fields. The corresponding densities,  $n_1 - n_{DP} = 1.15 \cdot 10^{12} \text{ cm}^{-2}$  and  $n_2 - n_{DP} = 3.4 \cdot 10^{12} \text{ cm}^{-2}$ , are smaller than in sample  $S_A$ . We do not expect to see the third conductance peak because  $n_3 - n_{DP} \simeq 6(n_1 - n_{DP}) \simeq 6.9 \cdot 10^{12} \text{ cm}^{-2}$  exceeds our experimental window  $n = \pm 6 \cdot 10^{12} \text{ cm}^{-2}$ . We conclude that the sequence of conductance peaks maps qualitatively well the prediction for massive surface states.

To put the analysis on a quantitative basis we extract the critical field  $\mathcal{E}_T = 2\pi\hbar v_F n_T/e$ . Here we have to recall that surface states contribute to a fraction of the measured compressibility and accordingly of the total TI charge in the presence of compressibility backgrounds (see Fig.3-d). We estimate this fraction to approximately half of the total charge in both samples with  $n_T^A \simeq (1.8 \pm 0.4) \cdot 10^{12} \text{ cm}^{-2}$  and  $n_T^B \simeq (0.6 \pm 0.1) \cdot 10^{12} \text{ cm}^{-2}$ . Taking  $v_F = 1.6 \cdot 10^6 \text{ ms}^{-1}$  from the compressibility of  $S_A$  (electron side), we deduce  $\mathcal{E}_T^A = (1.0 \pm 0.2) \cdot 10^8 \text{ Vm}^{-1}$ . With  $2\Delta_1 = 0.3 \text{ eV}$  (HgTe) and  $2\Delta_2 = 0.9 \text{ eV}$  ( $\text{Cd}_{0.7}\text{Hg}_{0.3}\text{Te}$ )

capping of  $S_A$ ) in Eq.(2) we obtain  $\xi \simeq (5 \pm 1)$  nm in agreement with theoretical simulations in Ref.[34]. Taking  $\varepsilon_{ins}^A = C_{inst_{ins}}/\varepsilon_0 \simeq 4.5$  (from Fig.3-a) and  $\varepsilon_{HgTe} \simeq 20$  Refs.[26,27] we deduce a large critical applied electric field  $\mathcal{E}_c^A \simeq 5 \cdot 10^8 \text{ Vm}^{-1}$ .

The same analysis can be carried out for the doped sample  $S_B$  where the Dirac point is shifted at  $\mathcal{E}_{DP} \simeq -1 \cdot 10^8 \text{ Vm}^{-1}$ , yielding  $\mathcal{E}_T^B = (0.4 \pm 0.1) \cdot 10^8 \text{ Vm}^{-1}$ . The fact that  $\mathcal{E}_T^B < \mathcal{E}_T^A$  highlights the importance of the capping layer in strengthening the robustness of surface topological states. Taking  $\varepsilon_{ins}^B \simeq 4.8$  (from Fig.3-b) we deduce  $\mathcal{E}_c^B = (1.5 \pm 0.3) \cdot 10^8 \text{ Vm}^{-1}$ . As a matter of fact we do observe in Fig.6-c a faint conductance peak at  $\mathcal{E}_{-1}^B = -1.4 \cdot 10^8 \text{ Vm}^{-1}$  close to  $-\mathcal{E}_c^B$  below the Dirac point. It signals the field-induced collapse of the first massive surface states in the hole doping regime. Note that with  $v_F \simeq 5 \cdot 10^5 \text{ ms}^{-1}$  (hole regime) the critical hole density  $n_T^B \simeq -1.8 \cdot 10^{12} \text{ cm}^{-2}$  is large and the  $m = -1$  conductance peak would not be observable in the absence of a strong electric field renormalization (factor  $1/\sqrt{1 - \beta^2} \simeq 3$ ). Above  $\mathcal{E}_c^B$  the conductivity becomes featureless in Fig.6-c, consistently with expectations for a normal semiconductor hetero-junction.

Finally we have plotted in Figs.6-(a,c) (solid black lines) the theoretical prediction for the quantum capacitance calculated using the calculated surface state density of states in Eq.(4). Here the agreement is only qualitative with two main deviations from experiment : i) the vanishing of  $C_Q$  at the Dirac point is not observed experimentally (see discussion above) and, ii) the predicted discontinuity of  $C_Q$  at the onset of the massive surface subbands is not observed and rather replaced by a bump (Fig.6-a) close to the resistance maximum at the mid MSS1 and MSS2 subband edges. This disagreement may reside in an experimental smearing due to combined effects of charge metastability and sample inhomogeneity.

We conclude to a semi quantitative agreement between theory and experiment with a strong evidence of excited topological surface subbands. The agreement is quite robust in the intrinsic sample  $S_A$  as the model parameters are strongly constrained : the material parameters  $2\Delta_1 = 0.3 \text{ eV}$ ,  $2\Delta_2 = 0.9 \text{ eV}$  and  $\varepsilon_{HgTe} \simeq 20$  are tabulated, the Fermi velocity  $v_F = 1.6 \cdot 10^6 \text{ eV}$  is measured independently, and the TSS penetration depth  $\xi \sim 5 \text{ nm}$  has been estimated numerically elsewhere [34]. With a smaller critical density  $n_T \simeq 0.6 \cdot 10^{12} \text{ cm}^{-2}$ , the uncapped sample  $S_B$  gives further insight into the  $m(m+1)/2$  sequence of excited states and provides some evidence on the existence of a critical electric field  $\mathcal{E}_c^B = 1.5 \cdot 10^8 \text{ Vm}^{-1}$ . Due to finite chemical doping ( $n_0 \simeq 2.6 \cdot 10^{12} \text{ cm}^{-2}$ ) the DP is shifted at  $\mathcal{E}_{DP}^B = -1 \cdot 10^8 \text{ Vm}^{-1}$  close to the critical field and partially smeared (the DP

resistance peak is barely larger than the scattering resistance peaks in Fig.4-b). This points to the existence of a critical doping above which the DP being pushed above the critical field becomes invisible and replaced by a field induced topological-to-normal transition at  $\mathcal{E}_c$ .

We note that massive excited surface states have also been reported in ARPES investigation of  $\text{Bi}_2\text{Se}_3$  crystals (see e.g. [38,39] and references therein). These samples were intentionally doped with potassium adatoms to increase surface doping (energy  $\mu \sim 0.6$  eV) and populate the excited states. This doping creates strong electric fields at the surface capable of confining a 2D electron gas (2DEG). The 2DEG scenario is supported in Ref.[39] by the observation of Rashba splitting and the agreement with numerical simulations. This interpretation does not hold for the high quality HgTe samples investigated here where doping is either negligible ( $\mu \lesssim 0.01$  eV in sample  $S_A$ ) or small ( $\mu \lesssim 0.15$  eV in sample  $S_B$ ). The MSSs reported here are likely intrinsic and concomitant to the Dirac topological surface states. Actually we cannot exclude that 2DEGs observed in  $\text{Bi}_2\text{Se}_3$  have a different origin but are similar in nature, *i.e.* linked to Dirac states. Further experimental and theoretical investigations are needed to settle this question.

## VI. CONCLUSION

Our experimental work provides a set of observables supporting the existence of excited surface states in the 3D topological insulator HgTe. We associate these states to the massive surface states (MSSs) confined by a smooth topological interface. Our experiment shows that MSSs eventually collapse at high fields  $\mathcal{E} \sim 10^8 \text{ Vm}^{-1}$  as predicted by theory.

Importantly our work highlights the relevance of the finite depth of the surface states and the role of finite bandgaps in the TI and its capping layer. This observation points to the relevance of a  $n - \mathcal{E}$  phase diagram for 3D TIs which constitutes a basis of further experimental investigations. As an example, we anticipate that by varying the insulator permittivity one can tune the capacitor charging line and map more precisely the diagram. In addition, by changing the capping layer (*i.e.*  $\Delta_2$ ) or the topological insulator (*i.e.*  $\Delta_1$ ) one can tune the critical field and further explore the interface model. We have explored this critical behavior by applying a large electric field but one could also investigate it by tuning electron-electron interactions, applying an external magnetic field, or simply by increasing

the temperature. The experimental approach can be readily expanded to other topological phases like Weyl semi-metals where topological effects extend in the bulk. As such this study provides new directions to improve the robustness of topological states which may turn important for quantum technology purposes [22].

## VII. APPENDIX : LORENTZ BOOST OF SURFACE STATES IN AN ELECTRIC FIELD

In section IV A we have introduced the Hamiltonian  $\hat{H}_s = \hat{H}'_{s0} + (V_0 - e\mathcal{E}z)\mathbb{1}$ . In order to deal with this new  $z$ -dependence, we perform a Lorentz boost on the time-independent Schrödinger equation  $e^{\frac{\eta}{2}\hat{J}}(\hat{H}'_s - \varepsilon\mathbb{1})e^{\frac{\eta}{2}\hat{J}}|\bar{\Psi}\rangle = 0$ , where the Lorentz boost [23] is realized by the hyperbolic transformation  $|\Psi'\rangle = \mathcal{N}e^{-\frac{\eta}{2}\hat{J}}|\Psi\rangle$  generated by  $\hat{J} = \sigma_y \otimes \sigma_x$ , in terms of the Pauli matrices  $\sigma_x$  and  $\sigma_y$ .

In the case  $\tanh(\eta) \equiv \beta = \mathcal{E}/\mathcal{E}_T \in [-1, 1]$  and  $V_0 = -\beta\Delta_1$ , one can thus make the  $(V_0 - e\mathcal{E}z)\mathbb{1}$ -term vanish in the comoving frame of reference. If we define the pseudo-magnetic field  $B = \mathcal{E}_T/v_F$ , this transformation can be understood from the viewpoint of *special relativity* as a boost to a frame of reference where the drift velocity  $v_D = \mathcal{E}/B$  vanishes [23]. The condition  $\mathcal{E}/\mathcal{E}_T = v_D/v_F \in [-1, 1]$  is similar to the existence of a limiting velocity, the Fermi velocity  $v_F$  plays the role of the speed of light in special relativity. The Schrödinger equation becomes  $\hat{H}'_s|\bar{\Psi}\rangle = \varepsilon|\bar{\Psi}\rangle$  with

$$\hat{H}'_s = \begin{bmatrix} \hbar v'_F k_x & \hbar v'_F k_y & 0 & \sqrt{2\hbar v'_F e\mathcal{E}'_T} \hat{b} \\ \hbar v'_F k_y & -\hbar v'_F k_x & \sqrt{2\hbar v'_F e\mathcal{E}'_T} \hat{b} & 0 \\ 0 & \sqrt{2\hbar v'_F e\mathcal{E}'_T} \hat{b}^\dagger & \hbar v'_F k_x & -\hbar v'_F k_y \\ \sqrt{2\hbar v'_F e\mathcal{E}'_T} \hat{b}^\dagger & 0 & -\hbar v'_F k_y & -\hbar v'_F k_x \end{bmatrix}, \quad (5)$$

with  $v'_F = \sqrt{1 - \beta^2}v_F$ ,  $\mathcal{E}'_T = (1 - \beta^2)\mathcal{E}_T$  and the ladder operators  $\hat{b}, \hat{b}^\dagger$  where

$$\hat{b} = \frac{1}{(1 - \beta^2)^{1/4} \sqrt{2\hbar v'_F e\mathcal{E}'_T}} \left\{ \hbar v_F k_x - i\sqrt{1 - \beta^2} \left[ e\mathcal{E}_T z - \left( \Delta_1 + \frac{\beta}{\beta^2 - 1} \varepsilon \right) \right] \right\}, \quad (6)$$

$$\hat{b}^\dagger = \frac{1}{(1 - \beta^2)^{1/4} \sqrt{2\hbar v'_F e\mathcal{E}'_T}} \left\{ \hbar v_F k_x + i\sqrt{1 - \beta^2} \left[ e\mathcal{E}_T z - \left( \Delta_1 + \frac{\beta}{\beta^2 - 1} \varepsilon \right) \right] \right\}. \quad (7)$$

As a consequence of the Lorentz boost, the ladder operators are now explicitly energy-dependent as well as the mean position of the number states  $\langle z \rangle = \left( \Delta_1 + \frac{\beta}{\beta^2 - 1} \varepsilon \right) / e\mathcal{E}_T$ .



For our theory to describe a surface state, this position must be within  $\langle z \rangle \in [0, \xi]$ , and one notices that for  $\beta \rightarrow 1$  this condition is not fulfilled for  $\varepsilon \neq 0$ .

The spectrum is found using states of the form  $|\Psi_{m,\mathbf{k}}\rangle = (\alpha_1|m\rangle, \alpha_2|l\rangle, \alpha_3|m-1\rangle, \alpha_4|m-1\rangle)$  for  $m \geq 1$  and  $|\Psi_{0,\mathbf{k}}\rangle = (\alpha_1|0\rangle, \alpha_2|0\rangle, 0, 0)$  for  $m = 0$ , in the comoving frame of reference. The  $|m\rangle$  states are the eigenstates of the number operator  $\hat{m} = \hat{b}^\dagger \hat{b}$ .

## Acknowledgments

We gratefully acknowledge B.A. Bernevig, N. Regnault, R. Ferreira, G. Bastard and M. Civelli for fruitful discussions.

---

\* Electronic address: bernard.placais@lpa.ens.fr

- <sup>1</sup> X.-L. Qi and S.-C. Zhang, *Rev. Mod. Phys.* **83**, 1057-1110 (2011). *Topological insulators and superconductors*
- <sup>2</sup> B. A. Bernevig, T. L. Hughes, S.-C. Zhang, *Science* **314**, 1757 (2006). *Quantum Spin Hall Effect and Topological Phase Transition in HgTe Quantum Wells*
- <sup>3</sup> L. Fu, C.L. Kane, E.J. Mele, *Phys. Rev. Lett.* **98**, 106803 (2007). *Topological insulators in three dimensions*
- <sup>4</sup> P. Hosur, X. Qi, *C. R. Physique* **14**, 857 (2013). *Recent developments in transport phenomena in Weyl semimetals*
- <sup>5</sup> S.Y. Xu, I. Belopolski, N. Alidoust, M. Neupane, G. Bian, C.L. Zhang, R. Sankar, G.Q. Chang, Z.J. Yuan, C.C. Lee, S.M. Huang, H. Zheng, J. Ma, D.S. Sanchez, B.K. Wang, A. Bansil, F.C. Chou, P.P. Shibayev, H. Lin, S. Jia, M.Z. Hasan, *Science* **349**, 6248 (2015). *Discovery of a Weyl fermion semimetal and topological Fermi arcs*
- <sup>6</sup> M. König, S. Wiedmann, C. Brune, A. Roth, H. Buhmann, L.W. Molenkamp, X.L. Qi, S.C. Zhang, *Science* **318**, 5851 (2007). *Quantum spin hall insulator state in HgTe quantum wells*
- <sup>7</sup> J. Wiedenmann, E. Bocquillon, R.S. Deacon, S. Hartinger, O. Herrmann, T.M. Klapwijk, L. Maier, C. Ames, C. Brune, C. Gould, A. Oiwa, K. Ishibashi, S. Tarucha, H. Buhmann, L.W. Molenkamp, *Nat. Comm.* **7**, 10303 (2016). *4 pi-periodic Josephson supercurrent in HgTe-based*

- <sup>8</sup> E. Bocquillon, R. S. Deacon, J. Wiedenmann, P. Leubner, T. M. Klapwijk, C. Brune, K. Ishibashi, H. Buhmann, L. W. Molenkamp *Nat. Nanotech.* **12**, 137 (2017). *Gapless Andreev bound states in the quantum spin Hall insulator HgTe*
- <sup>9</sup> R. S. Deacon, J. Wiedenmann, E. Bocquillon, F. Domnguez, T. M. Klapwijk, P. Leubner, C. Brune, E. M. Hankiewicz, S. Tarucha, K. Ishibashi, H. Buhmann, L. W. Molenkamp *arXiv*, 1603.09611 (2016). *Josephson radiation from gapless Andreev bound states in HgTe-based topological junctions*
- <sup>10</sup> L. Wu, M. Salehi, N. Koirala, J. Moon, S. Oh, N. P. Armitage, *Science* **354**, 1124 (2016). *Quantized Faraday and Kerr rotation and axion electrodynamics of the surface states of three-dimensional topological insulators*
- <sup>11</sup> V. Dziom, A. Shuvaev, A. Pimenov, G. V. Astakhov, C. Ames, K. Bendias, J. Böttcher, G. Tkachov, E. M. Hankiewicz, C. Brüne, H. Buhmann, and L. W. Molenkamp, *arXiv:arXiv:1603.05482v1* (2016). *Observation of the universal magnetoelectric effect in a 3D topological insulator*
- <sup>12</sup> S. N. Kempkes, A. Quelle, C. Morais Smith *Sci. Rep.* **6**, 38530 (2016). *Universalities of thermodynamic signatures in topological phases*
- <sup>13</sup> T. Kernreiter, M. Governale, U. Zülicke *Phys. Rev. B* **93**, 241304(R) (2016). *Quantum capacitance of an HgTe quantum well as an indicator of the topological phase*
- <sup>14</sup> B. Placais, P. Mathieu, Y. Simon, E.B. Sonin, K.B. Traito, *Phys. Rev. B* **54**, 13083 (1996). *Continuum electrodynamics of type-II superconductors in the mixed state: The dc and ac response*
- <sup>15</sup> N. Lutke-Entrup, B. Placais, P. Mathieu, Y. Simon, *Phys. Rev. Lett.* **79**, 2538 (1997). *Depinning transition in type-II superconductors*
- <sup>16</sup> N. Lutke-Entrup, B. Placais, P. Mathieu, Y. Simon, *Physica B* **255**, 75 (1998). *RF-studies of vortex dynamics in isotropic type-II superconductors*
- <sup>17</sup> C. Brüne, C.X. Liu, E.G. Novik, E. M. Hankiewicz, H. Buhmann, Y.L. Chen, X.L. Qi, Z.X. Shen, S.C. Zhang, L. W. Molenkamp, *Phys. Rev. Lett.* **106**, 126803 (2011). *Quantum Hall Effect from the Topological Surface States of Strained Bulk HgTe*
- <sup>18</sup> D. A. Kozlov, D. Kvon, E. B. Olshanetsky, N. N. Mikhailov, S. A. Dvoretzky, D. Weiss, *Phys. Rev. Lett.* **112**, 196801 (2014). *Transport Properties of a 3D Topological Insulator based on a*

- <sup>19</sup> C. Brüne, C. Thienel, M. Stuißer, J. Böttcher, H. Buhmann, E.G. Novik, C.-X. Liu, E.M. Hankiewicz, L. W. Molenkamp, *Phys. Rev. X* **4**, 041045 (2014). *Dirac-Screening Stabilized Surface-State Transport in a Topological Insulator*
- <sup>20</sup> S. Xu, Y. Han, X. Chen, Z. Wu, L. Wang, T. Han, W. Ye, H. Lu, G. Long, Y. Wu, J. Lin, Y. Cai, K. M. Ho, Y. He, N. Wang, *Nano Lett.* **15**, 2645 (2015). *van der Waals Epitaxial Growth of Atomically Thin Bi<sub>2</sub>Se<sub>3</sub> and Thickness-Dependent Topological Phase Transition*
- <sup>21</sup> D. A. Kozlov, D. Bauer, J. Ziegler, R. Fischer, M. L. Savchenko, Z. D. Kvon, N. N. Mikhailov, S. A. Dvoretzky, D. Weiss, *Phys. Rev. Lett.* **116**, 166802 (2016). *Probing Quantum Capacitance in a 3D Topological Insulator*
- <sup>22</sup> T. Karzig, G. Refael, F. von Oppen *Phys. Rev. X* **3**, 041017 (2013). *Boosting Majorana Zero Modes*
- <sup>23</sup> V. Lukose, R. Shankar and G. Baskaran, *Phys. Rev. Lett.* **98**, 116802 (2007). *Novel Electric Field Effects on Landau Levels in Graphene*
- <sup>24</sup> Y. Guldner, C. Rigaux, M. Grynberg, A. Mycielski, *Phys. Rev. B* **8**, 3875 (1973). *Interband Magneto-absorption in HgTe*
- <sup>25</sup> K. Bendias, R. Schlereth, C. Brüne, H. Buhmann, in preparation (2017).
- <sup>26</sup> J. Baars, F. Sorger, *Solid State Communications* **10**, 875 (1972). *Reststrahlen spectra of HgTe and Cd<sub>x</sub>Hg<sub>1-x</sub>Te*
- <sup>27</sup> P. Capper, J. Garland, editors. *Mercury Cadmium Telluride: Growth, Properties and Applications*. Wiley, 2010.
- <sup>28</sup> D. Neumaier, *private communication* (2015).
- <sup>29</sup> E. Pallecchi, A.C. Betz, J. Chaste, G. Fève, B. Huard, T. Kontos, J.-M. Berroir, B. Plaçais, *Phys. Rev. B* **83**, 125408 (2011). *Transport scattering time probed through rf admittance of a graphene capacitor*
- <sup>30</sup> C. Liu, G. Bian, T.-R. Chang, K. Wang, S.-Y. Xu, I. Belopolski, I. Miotkowski, H. Cao, K. Miyamoto, C. Xu, C. E. Matt, T. Schmitt, N. Alidoust, M. Neupane, H.-T. Jeng, H. Lin, A. Bansil, V. N. Strocov, M. Bissen, A. V. Fedorov, X. Xiao, T. Okuda, Y. P. Chen, M. Z. Hasan, *Phys. Rev. B* **92**, 115436 (2015). *Tunable spin helical Dirac quasiparticles on the surface of three-dimensional HgTe*
- <sup>31</sup> Q. Wilmart, A. Inhofer, M. Boukhicha, W. Yang, M. Rosticher, P. Morfin, N. Garroum, G. Fève,

- J.-M. Berroir, B. Plaais *Scientific Reports* **6**, 21085 (2016). *Contact gating at GHz frequency in graphene*
- <sup>32</sup> S. Tchoumakov, M. Civelli and M.O. Goerbig, *arXiv*: arXiv:1612.07693 (2016). *Magnetic description of the Fermi arc in type-I and type-II Weyl semimetals*
- <sup>33</sup> M.O. Goerbig, *arXiv*: arXiv:0909.1998v2 (2009). *Quantum Hall Effects*
- <sup>34</sup> Y. Baum, J. Böttcher, C. Brüne, C. Thienel, L. W. Molenkamp, A. Stern, E. M. Hankiewicz, *Phys. Rev. B* **89**, 245136 (2014). *Self-consistent  $k$   $p$  calculations for gated thin layers of three-dimensional topological insulators*
- <sup>35</sup> J. Linder, T. Yokoyama, A. Sudbo, *Phys. Rev. B* **80**, 205401 (2009). *Anomalous finite size effects on surface states in the topological insulator Bi<sub>2</sub>Se<sub>3</sub>*
- <sup>36</sup> G. Bastard. *Wave mechanics applied to semiconductor heterostructures*. Les éditions de Physique - Monographies de Physique, 1996.
- <sup>37</sup> E. Novik, A. Pfeuffer-Jeschke, T. Jungwirth, V. Latussek, C. Becker, G. Landwehr, H. Buhmann, and L. Molenkamp, *Physical Review B* **72**, 035321 (2005).
- <sup>38</sup> M. Bianchi, D. Guan, S. Bao, J. Mi, B. Brummerstedt Iversen, P.D.C. King, P. Hofmann, *Nat. Comm.* **3**, 1159 (2012). *Coexistence of the topological state and a two-dimensional electron gas on the surface of Bi<sub>2</sub>Se<sub>3</sub>*
- <sup>39</sup> M.S. Bahramy, P.D.C. King, A. de la Torre, J. Chang, M. Shi, L. Patthey, G. Balakrishnan, Ph. Hofmann, R. Arita, N. Nagaosa<sup>1</sup>, F. Baumberger, *Nat. Comm.* **3**, 1159 (2012). *Emergent quantum confinement at topological insulator surfaces*
- <sup>40</sup> L. Veyrat, F. Iacovella, J. Dufouleur, C. Nowka, H. Funke, M. Yang, W. Escoffier, M. Goiran, B. Eichler, O.G. Schmidt, B. Buchner, S. Hampel, R. Giraud, *Nano Lett.* **15**, 7503 (2015). *Band Bending Inversion in Bi<sub>2</sub>Se<sub>3</sub> Nanostructures*
- <sup>41</sup> D. Culcer, E.H. Hwang, T.D. Stanescu, S. das Sarma, *Phys. Rev. B* **82**, 155457 (2010). *Two-dimensional surface charge transport in topological insulators.*
- <sup>42</sup> The resurgence of a bulk contribution in the vicinity of a Dirac point is expected however, due to the vanishing Dirac screening at TSS neutrality, illustrated by the divergence of the effective screening length  $\lambda = \varepsilon/C_Q$ . Such effects have been recently demonstrated in gated graphene-on-metal contacts [31]. The analog of TIs would be the case of graphene-on-semiconductor, where the finite compressibility of the small gap semiconductor is taken into account. This case, which has not been investigated yet, is beyond the scope of our paper that focusses on the high field

regime. In the following we shall therefore focus on the electron-doped regime and subtract a background compressibility  $\sim 0.01 \text{ Fm}^{-2}$ .